IEEE Access
Multidisciplinary | Rapid Review | Open Access Journal

Received May 27, 2018, accepted June 27, 2018, date of publication July 2, 2018, date of current version July 25, 2018.

Digital Object Identifier 10.1109/ACCESS.2018.2851948

Surface Reconstruction Adopting Laser Plane of Linear Path System Registered by Parallel Constraint

GUAN XU[1], (Member, IEEE), FANG CHEN[1], XIAOTAO LI[2], AND JUNYI CHEN[1]
[1]Department of Vehicle Operation Engineering, Transportation College, Jilin University, Changchun 130025, China
[2]School of Mechanical Science and Engineering, Jilin University, Nanling Campus, Changchun 130025, China

Corresponding author: Xiaotao Li (lixiaotao@jlu.edu.cn)

This work was supported in part by the National Natural Science Foundation of China under Grant 51478204 and Grant 51205164 and in part by the Natural Science Foundation of Jilin Province under Grant JC20170101214 and Grant JC20150101027.

ABSTRACT A surface reconstruction technology, which is contributed from the parallel constraint between two laser planes, is introduced and achieved by a laser projector guided by a linear path system. The projection geometry is constructed by the projection planes, the target planes, the laser planes, the image planes, and the intersection lines. First, the angle between the direction of the projector translation and the normal vector of the laser plane is contributed by the bilinear product operator of the intersection line and the projection matrix. Second, the distance errors are generated from the points on two laser planes and parameterized by the angle and the laser plane for the optimization. Finally, the surface reconstruction is realized by the optimized angle and laser plane. The experiments are conducted to prove the validity of the surface measurement method. The mean of the reconstruction errors is 0.78 mm in the test, which indicates the application potentials from the experimental investigations.

INDEX TERMS Surface reconstruction, structured light, calibration.

I. INTRODUCTION

Surface reconstruction of 3D object is an absorbing study in the research field of the optical measurement [1]–[3]. The aim of the study is to provide the 3D shape of an object, which is an effective approach to understand the real structure in the world [4], [5]. Thus, the surface reconstruction method is widely described in the technologies of medical and industrial applications [6]–[9].

The previous works of the surface reconstruction with respect to the camera are classified into two types: passive reconstruction and active reconstruction. In the passive reconstruction, as a camera captures only one 2D image, the other camera is employed to capture the other 2D image [10]. Then the 3D information of an object is acquired by the feature matching and projection geometry [11]. The reconstruction method is based on the stereo vision. Kieu *et al.* [12] presents an accurate method to build the 3D surface of an object by the stereo vision. In the method, the scale-invariant feature transform (SIFT) [13] is employed to extract the feature points in the images and match them correctly. Then a registration method in the full view-field is adopted to match the points in the subpixel accuracy. The 3D surface is reconstructed by the matching points and calibrated cameras. Sandoz *et al.* [14] proposes a stereo-vision method for the visual measurement of the position and orientation of a target. The pseudo-periodic pattern (PPP) is designed on the target to facilitate the image processing by phase calculations. The test results of the position and orientation are reported in the paper. Shao *et al.* [15] outlines a stereo-vision-based method to measure the deformation of the large engineering structure. The stereo-digital image correlation (stereo-DIC) is developed to obtain the non-intrusive characteristic in the measurement. Luo *et al.* [16] provides a stereo vision method to solve the 3D pose of an object. The intersection point of the contour line is chosen as the feature points and the epipolar constraint is employed in the estimation. As only the natural light on object is reflected to the cameras, the surface reconstructions above are the passive processes, which tend to be impacted by the stochastic illumination. Furthermore, the feature matching is a difficult problem for the smooth surface without evident texture. Hence, the passive reconstruction is valid for the rough surface or the surface with texture.

In order to overcome the shortcoming of the passive reconstruction, the illumination from a projector is chosen as the non-touch, active mark on the measured object [17], [18]. The projector can be regarded as an active camera. Huang *et al.* [19] describes a method with the polarization-coded structured light to improve the 3D reconstruction in the ambient illumination. Shi and Liang [20] reports a surface reconstruction method for the object processed by the coating spray. A flexible coordinate control network (CNN) is achieved to adjust the whole-field accuracy. There are also active reconstruction methods based on the linear path system. Villa *et al.* [21] presents a transformation from the structured-light phase to the 3D coordinate of measured object. The structured-light phase is calibrated by a flat target on a linear path stage, which is moved to different positions. In the calibration, as the coded light is project on the flat target, the light code on the target changes with different movement displacement of the linear path stage. The slope of the phase-time is proportional to the known displacement. Therefore, a fifth order polynomial fitting is chosen to determine the relationship between the displacement and the coded light on the flat target. The Fourier transform is employed to determine the 3D points on the object. The linear stage is also employed by Hu and Huang [22] in order to acquire the projection images of the plate on different positions and calibrate the geometrical parameters of the surface measurement system. A spot is project to the plate on the stage for the measurement of the distance parameter and angle parameter. The linear path stage in the previous works takes a flat plate on the stage. The movement of the plate is derived from the motorized linear stage. However, the linear path stage in the method is employed to motor the laser projector. Then, the linear path stage in the previous works contributes the standard displacement of the plate for the system calibration. The standard displacement relates to the size of the light marks on the plate. However, the linear path stage here provides the standard displacement of the laser projector for both the system calibration and reconstruction. The method takes the advantage of the parallel constraint from the linear path stage. Moreover, the structured-light methods above are based on the coded gratings from the digital light processing (DLP) projector, which tends to be more influenced by illuminations than the laser plane from the laser projector. In the paper, a reconstruction method is achieved by the laser plane motored and positioned by the linear path system. The calibration and reconstruction are realized by the movement of the linear path system. The laser plane is registered by the parallel constraint of the linear path and optimized by the standard distances on the laser planes. The high reconstruction accuracy is contributed by the laser plane positioned by the step motor.

The following paper includes three parts. Section 2 describes the camera-laser-plane system that is guided by a stepper motor and rails. Then the projection geometry is outlined in the reconstruction model. The angle between the direction of the table translation and the normal vector of the laser plane as well as the laser plane is initialized by the bilinear product operator of the intersection laser line and the projection matrix. The angle and laser plane are optimized by the parallel constraint and two distances on two laser planes. The aim of Section 3 is to verify the surface reconstruction method by the experiments. The surfaces of different objects are recovered in the experiments. Section 4 summarizes the paper.

II. RECONSTRUCTION APPROACH

A camera-laser-plane system that is guided by a stepper motor and rails is constructed to perform the surface reconstruction. The reconstruction model is illustrated in Fig. 1. A test system consists of a camera, a laser projector on the table, a stepper motor and guide rails. The stepper motor is controlled by the digital stepping driver. The computer with the I/O card sends pluses to the digital stepping driver. Then, the guide screw rotates with the output shaft of the stepper motor. The laser projector on the stage moves along the rails. Thus, the laser planes are parallel to each other. 1D, 2D and 3D targets are reported for the calibration in computer-vision-measurement. The 1D target benefits for the easy manufacture. However, the calibration with 1D target should satisfy the strict movement conditions. The 3D target is made by three vertical plates and difficult to be manufactured. Therefore, considering the easy manufacture of the target and the flexible movement, a convenient 2D target, a plate with the texture, is employed to perform the calibration of the measurement system. 15 positions of the target are tested in the calibration process. The laser plane moves from the starting position to the second position. In system calibration, the laser planes are projected on the 2D target in different positions. Therefore, several laser lines are generated from the intersections and also captured by the camera. As the translation value of the linear path system is derived from the pulses of the computer, the angle between the direction of the table translation and the normal vector of the laser plane is solved by the laser planes in position I and position II.

The geometrical model is represented by Fig. 2. The camera, image and world coordinate systems are represented by O_1-$X_1Y_1Z_1$, O_2-X_2Y_2, O_3-$X_3Y_3Z_3$ and fixed on the camera, image and target, respectively. As the world coordinate system moves with the target, the fixed camera coordinate system is treated as the global coordinate system where all the geometrical variables are transformed.

The i-th-position target plane $\boldsymbol{\Psi}_{\mathrm{tc}}^{i} = (\psi_{\mathrm{tc},1}^{i}, \psi_{\mathrm{tc},2}^{i}, \psi_{\mathrm{tc},3}^{i}, \psi_{\mathrm{tc},4}^{i})^{\mathrm{T}}$ in the camera coordinate system is generated from the target plane in the world coordinate system as [23]

$$\boldsymbol{\Psi}_{\mathrm{tc}}^{i} = (\mathrm{H}_{\mathrm{w}}^{i})^{-\mathrm{T}} \boldsymbol{\Psi}_{\mathrm{tw}} \tag{1}$$

where $\mathrm{H}_{\mathrm{w}}^{i}$ is the homography from the world coordinate system to the camera coordinate system and derived from the Zhang's method [24]. $\boldsymbol{\psi}_{\mathrm{tw}} = (0, 0, 1, 0)^{\mathrm{T}}$ is the coordinate of the target plane in the world coordinate system.

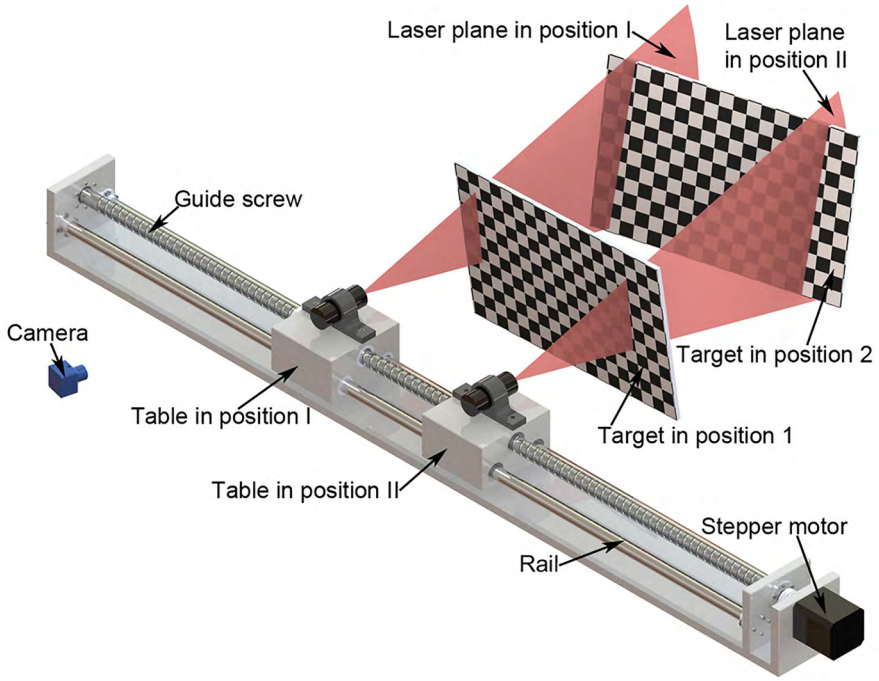

FIGURE 1. Calibration approach of a camera-laser-plane system that is guided by a stepper motor and rails.

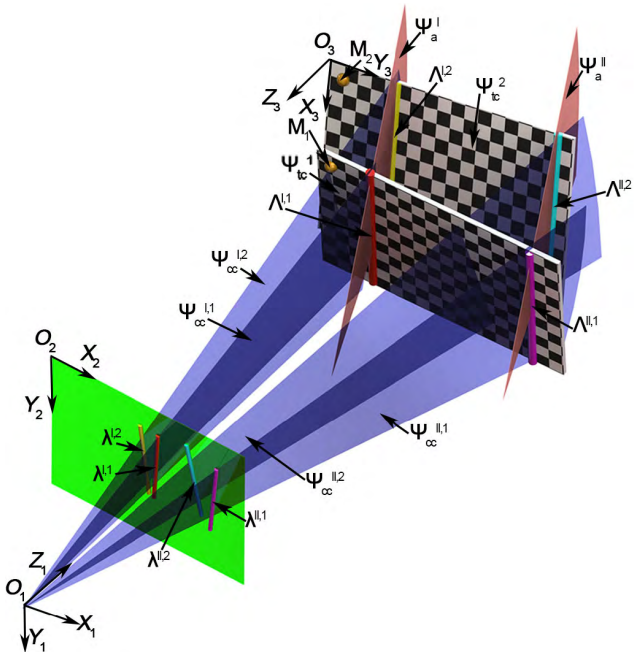

FIGURE 2. Projection geometry of the projection planes, the target planes, the laser planes, the image plane and the intersection lines.

The projection plane $\Psi_{cc}^{I,i}$ $(i = 1, 2, \ldots, n)$ is determined by [23]

$$\Psi_{cc}^{I,i} = (H_w^i)^{-T}(P^i)^T \lambda^{I,i} \tag{2}$$

where P_i is the projection transform from the world coordinate system to the image coordinate system [24]. $\lambda^{I,i}$ is the mapping of the intersection line between the laser plane on the I-st position and the target on the i-th position. The closed form solution of the laser plane Ψ_a^I has been obtained from the singular value decomposition (SVD) method in [23]. Therefore, we focus on the approach to improve the accuracy of the laser plane by the parallel constraint of the linear path system.

In order to rebuild the object surface by a laser plane on the second position, the laser plane Ψ_a^I on the I-st position is translated to the laser plane Ψ_a^{II} on the II-nd position. Ψ_a^{II} is parallel to Ψ_a^I and denoted by $\Psi_a^{II} = (\psi_{a,1}^I, \psi_{a,2}^I, \psi_{a,3}^I, \psi_{a,4}^{II})^T$ consequently. The displacement of the laser plane in the direction of the normal vector of the laser plane can be given by the projection of the known table translations. It also can be expressed by the coordinates of two laser planes Ψ_a^I, Ψ_a^{II}. Accordingly, we have the relationship

$$s\cos\delta = (\psi_{a,4}^{II} - \psi_{a,4}^I)[(\psi_{a,1}^I)^2 + (\psi_{a,2}^I)^2 + (\psi_{a,3}^I)^2]^{-1/2} \tag{3}$$

where δ is the unknown angle between the direction of the table translation and the normal vector of the laser plane. Figure 3 illustrates the process to solve the angle δ by the following steps.

Figure 4 outlines the optimization process with the solutions of the angle δ and the coordinate of the laser plane Ψ_a^I From Eq. (3), the laser plane Ψ_a^{II} is denoted by

$$\Psi_a^{II} = (\psi_{a,1}^I, \psi_{a,2}^I, \psi_{a,3}^I, \psi_{a,4}^I + [(\psi_{a,1}^I)^2 + (\psi_{a,1}^I)^2 + (\psi_{a,1}^I)^2]^{1/2} s\cos\delta)^T \tag{4}$$

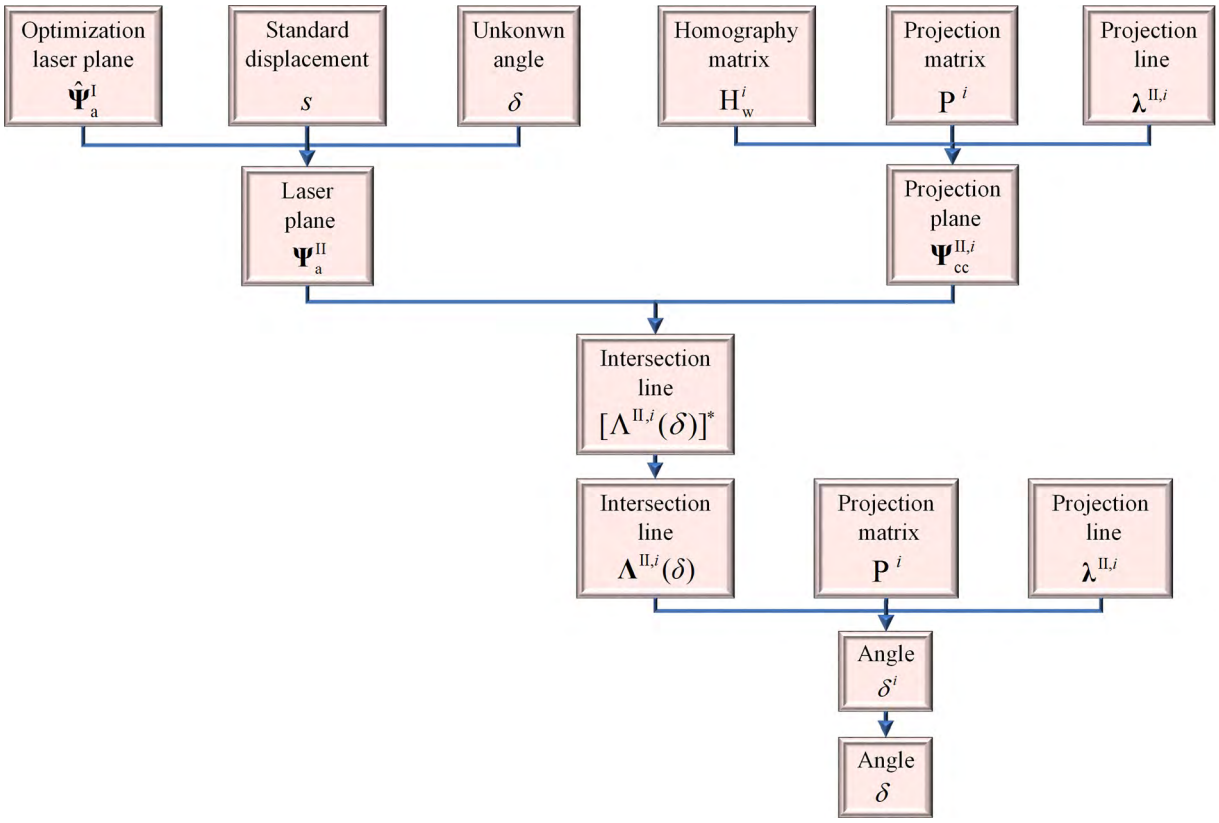

FIGURE 3. Registration process of the angle δ between the direction of the table translation and the normal vector of the laser plane.

The Plücker matrix $(\Lambda^{\mathrm{II},i})^*$ of the intersection line between the laser plane on the II-nd position and the projection plane is parameterized by the unknown angle δ as

$$[\Lambda^{\mathrm{II},i}(\delta)]^* = \boldsymbol{\Psi}_{\mathrm{a}}^{\mathrm{II}}(\delta)(\boldsymbol{\Psi}_{\mathrm{cc}}^{\mathrm{II},i})^{\mathrm{T}} - \boldsymbol{\Psi}_{\mathrm{cc}}^{\mathrm{II},i}[\boldsymbol{\Psi}_{\mathrm{a}}^{\mathrm{II}}(\delta)]^{\mathrm{T}} \tag{5}$$

where the projection plane $\boldsymbol{\Psi}_{\mathrm{cc}}^{\mathrm{II},i} = (\psi_{\mathrm{cc}}^{\mathrm{II},i}, \psi_{\mathrm{cc}}^{\mathrm{II},i}, \psi_{\mathrm{cc}}^{\mathrm{II},i}, \psi_{\mathrm{cc}}^{\mathrm{II},i})^{\mathrm{T}}$.

According to Eqs. (2) and (5) and the proportion of the Plücker matrix, the parameterized Plücker coordinate of the intersection laser line is

$$\boldsymbol{\Lambda}^{\mathrm{II},i}(\delta) = \{\mu_{12}^{\mathrm{II},i},\ \mu_{13}^{\mathrm{II},i},\ \mu_{14}^{\mathrm{II},i}(\delta),\ \mu_{23}^{\mathrm{II},i},\ \mu_{42}^{\mathrm{II},i}(\delta),\ \mu_{34}^{\mathrm{II},i}(\delta)\} \tag{6}$$

where

$$\begin{aligned}
\mu_{12}^{\mathrm{II},i} &= \psi_{\mathrm{a},1}^{\mathrm{I}}\psi_{\mathrm{cc},2}^{\mathrm{II},i} - \psi_{\mathrm{cc},1}^{\mathrm{II},i}\psi_{\mathrm{a},2}^{\mathrm{I}},\\
\mu_{13}^{\mathrm{II},i} &= \psi_{\mathrm{a},1}^{\mathrm{I}}\psi_{\mathrm{cc},3}^{\mathrm{II},i} - \psi_{\mathrm{cc},1}^{\mathrm{II},i}\psi_{\mathrm{a},3}^{\mathrm{I}},\\
\mu_{23}^{\mathrm{II},i} &= \psi_{\mathrm{a},2}^{\mathrm{I}}\psi_{\mathrm{cc},3}^{\mathrm{II},i} - \psi_{\mathrm{cc},2}^{\mathrm{II},i}\psi_{\mathrm{a},3}^{\mathrm{I}},\\
\mu_{14}^{\mathrm{II},i}(\delta) &= \psi_{\mathrm{a},1}^{\mathrm{I}}\psi_{\mathrm{cc},4}^{\mathrm{II},i} - \psi_{\mathrm{cc},1}^{\mathrm{II},i}\{\psi_{\mathrm{a},4}^{\mathrm{I}} + [(\psi_{\mathrm{a},1}^{\mathrm{I}})^2 + (\psi_{\mathrm{a},2}^{\mathrm{I}})^2\\
&\qquad + (\psi_{\mathrm{a},3}^{\mathrm{I}})^2]^{1/2} s\cos\delta\},\\
\mu_{42}^{\mathrm{II},i}(\delta) &= -\psi_{\mathrm{cc},4}^{\mathrm{II},i}\psi_{\mathrm{a},2}^{\mathrm{I}} + \psi_{\mathrm{cc},2}^{\mathrm{II},i}\{\psi_{\mathrm{a},4}^{\mathrm{I}} + [(\psi_{\mathrm{a},1}^{\mathrm{I}})^2 + (\psi_{\mathrm{a},2}^{\mathrm{I}})^2\\
&\qquad + (\psi_{\mathrm{a},3}^{\mathrm{I}})^2]^{1/2} s\cos\delta\},\\
\mu_{34}^{\mathrm{II},i}(\delta) &= \psi_{\mathrm{a},3}^{\mathrm{I}}\psi_{\mathrm{cc},4}^{\mathrm{II},i} - \psi_{\mathrm{cc},3}^{\mathrm{II},i}\{\psi_{\mathrm{a},4}^{\mathrm{I}} + [(\psi_{\mathrm{a},1}^{\mathrm{I}})^2 + (\psi_{\mathrm{a},2}^{\mathrm{I}})^2\\
&\qquad + (\psi_{\mathrm{a},3}^{\mathrm{I}})^2]^{1/2} s\cos\delta\}.
\end{aligned}$$

The Plücker coordinate of the intersection laser line is projected to the image plane to solve the unknown angle δ and then

$$\boldsymbol{\lambda}^{\mathrm{II},i} = \begin{bmatrix} \mathrm{P}^{2,i} \wedge \mathrm{P}^{3,i} | \boldsymbol{\Lambda}^{\mathrm{II},i}(\delta) \\ \mathrm{P}^{3,i} \wedge \mathrm{P}^{1,i} | \boldsymbol{\Lambda}^{\mathrm{II},i}(\delta) \\ \mathrm{P}^{1,i} \wedge \mathrm{P}^{2,i} | \boldsymbol{\Lambda}^{\mathrm{II},i}(\delta) \end{bmatrix} \tag{7}$$

where $\wedge$ is the operator of the Plücker coordinate that consists of the left plane and right plane. $|$ is the bilinear product operator [25]. $\boldsymbol{\lambda}^{\mathrm{II},i} = (\lambda_1^{\mathrm{II},i}, \lambda_2^{\mathrm{II},i}, \lambda_3^{\mathrm{II},i})^{\mathrm{T}}$ is the projection line of $\boldsymbol{\Lambda}^{\mathrm{II},i}(\delta)$ in the image. $\mathrm{P}^i = [(\mathrm{P}^{1,i})^{\mathrm{T}}, (\mathrm{P}^{2,i})^{\mathrm{T}}, (\mathrm{P}^{3,i})^{\mathrm{T}}]_{3\times 4}^{\mathrm{T}}$ is the projection matrix of the camera. Let

$$\begin{aligned}
\{q_{12}^{23,i}, q_{13}^{23,i}, q_{14}^{23,i}, q_{23}^{23,i}, q_{42}^{23,i}, q_{34}^{23,i}\} &= \mathrm{P}^{2,i} \wedge \mathrm{P}^{3,i},\\
\{q_{12}^{31,i}, q_{13}^{31,i}, q_{14}^{31,i}, q_{23}^{31,i}, q_{42}^{31,i}, q_{34}^{31,i}\} &= \mathrm{P}^{3,i} \wedge \mathrm{P}^{1,i},\\
\{q_{12}^{12,i}, q_{13}^{12,i}, q_{14}^{12,i}, q_{23}^{12,i}, q_{42}^{12,i}, q_{34}^{12,i}\} &= \mathrm{P}^{1,i} \wedge \mathrm{P}^{2,i}.
\end{aligned}$$

For the target on the i-th position, Eq. (7) contributes three equations of the unknown angle δ. Stacking the three equations, then

$$\delta^i = \arccos[\frac{1}{3}(Q_1^i + Q_2^i + Q_3^i)] \tag{8}$$

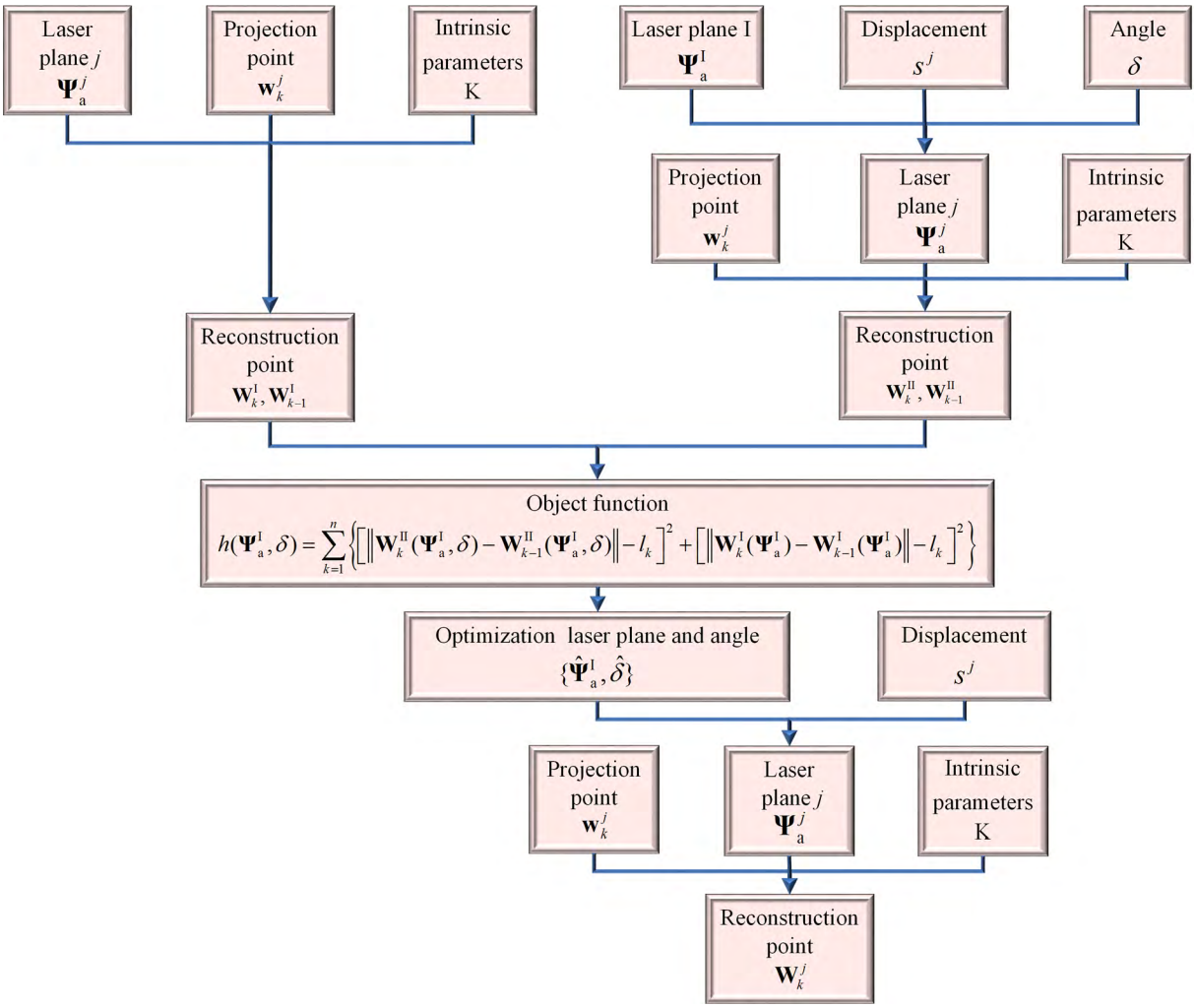

FIGURE 4. Reconstruction process with the angle δ and the laser plane that are optimized by the distances from two laser planes.

where

$$\begin{aligned}
Q_1^i = \{&[\lambda_1^{\mathrm{II},i} - q_{12}^{23,i}\psi_{\mathrm{a},3}^{\mathrm{I}}\psi_{\mathrm{cc},4}^{\mathrm{II},i} - q_{34}^{23,i}(\psi_{\mathrm{a},1}^{\mathrm{I}}\psi_{\mathrm{cc},2}^{\mathrm{II},i} - \psi_{\mathrm{cc},1}^{i}\psi_{\mathrm{a},2}^{\mathrm{I}}) \\
&+ q_{13}^{23,i}\psi_{\mathrm{cc},4}^{\mathrm{II},i}\psi_{\mathrm{a},2}^{\mathrm{I}} - q_{42}^{23,i}(\psi_{\mathrm{a},1}^{\mathrm{I}}\psi_{\mathrm{cc},3}^{\mathrm{II},i} - \psi_{\mathrm{cc},1}^{\mathrm{II},i}\psi_{\mathrm{a},3}^{\mathrm{I}}) \\
&- q_{14}^{23,i}(\psi_{\mathrm{a},2}^{\mathrm{I}}\psi_{\mathrm{cc},3}^{\mathrm{II},i} - \psi_{\mathrm{cc},2}^{\mathrm{II},i}\psi_{\mathrm{a},3}^{\mathrm{I}}) - q_{23}^{23,i}\psi_{\mathrm{a},1}^{\mathrm{I}}\psi_{\mathrm{cc},4}^{\mathrm{II},i}] \\
&\times (-q_{12}^{23,i}\psi_{\mathrm{cc},3}^{\mathrm{II},i} + q_{13}^{23,i}\psi_{\mathrm{cc},2}^{\mathrm{II},i} - q_{23}^{23,i}\psi_{\mathrm{cc},1}^{\mathrm{II},i})^{-1} - \psi_{\mathrm{a},4}^{\mathrm{I}}\} \\
&\times \{[(\psi_{\mathrm{a},1}^{\mathrm{I}})^2 + (\psi_{\mathrm{a},2}^{\mathrm{I}})^2 + (\psi_{\mathrm{a},3}^{\mathrm{I}})^2]^{1/2}s\}^{-1}, \\
Q_2^i = \{&[\lambda_2^{\mathrm{II},i} - q_{12}^{31,i}\psi_{\mathrm{a},3}^{\mathrm{I}}\psi_{\mathrm{cc},4}^{\mathrm{II},i} - q_{34}^{31,i}(\psi_{\mathrm{a},1}^{\mathrm{I}}\psi_{\mathrm{cc},2}^{\mathrm{II},i} - \psi_{\mathrm{cc},1}^{\mathrm{II},i}\psi_{\mathrm{a},2}^{\mathrm{I}}) \\
&+ q_{13}^{31,i}\psi_{\mathrm{cc},4}^{\mathrm{II},i}\psi_{\mathrm{a},2}^{\mathrm{I}} - q_{42}^{31,i}(\psi_{\mathrm{a},1}^{\mathrm{I}}\psi_{\mathrm{cc},3}^{\mathrm{II},i} - \psi_{\mathrm{cc},1}^{\mathrm{II},i}\psi_{\mathrm{a},3}^{\mathrm{I}}) \\
&- q_{14}^{31,i}(\psi_{\mathrm{a},2}^{\mathrm{I}}\psi_{\mathrm{cc},3}^{\mathrm{II},i} - \psi_{\mathrm{cc},2}^{\mathrm{II},i}\psi_{\mathrm{a},3}^{\mathrm{I}}) - q_{23}^{31,i}\psi_{\mathrm{a},1}^{\mathrm{I}}\psi_{\mathrm{cc},4}^{\mathrm{II},i}] \\
&\times (-q_{12}^{31,i}\psi_{\mathrm{cc},3}^{\mathrm{II},i} + q_{13}^{31,i}\psi_{\mathrm{cc},2}^{\mathrm{II},i} - q_{23}^{31,i}\psi_{\mathrm{cc},1}^{\mathrm{II},i})^{-1} - \psi_{\mathrm{a},4}^{\mathrm{I}}\} \\
&\times \{[(\psi_{\mathrm{a},1}^{\mathrm{I}})^2 + (\psi_{\mathrm{a},2}^{\mathrm{I}})^2 + (\psi_{\mathrm{a},3}^{\mathrm{I}})^2]^{1/2}s\}^{-1}, \\
Q_3^i = \{&[\lambda_3^{\mathrm{II},i} - q_{12}^{12,i}\psi_{\mathrm{a},3}^{\mathrm{I}}\psi_{\mathrm{cc},4}^{\mathrm{II},i} - q_{34}^{12,i}(\psi_{\mathrm{a},1}^{\mathrm{I}}\psi_{\mathrm{cc},2}^{\mathrm{II},i} - \psi_{\mathrm{cc},1}^{\mathrm{II},i}\psi_{\mathrm{a},2}^{\mathrm{I}}) \\
&+ q_{13}^{12,i}\psi_{\mathrm{cc},4}^{\mathrm{II},i}\psi_{\mathrm{a},2}^{\mathrm{I}} - q_{42}^{12,i}(\psi_{\mathrm{a},1}^{\mathrm{I}}\psi_{\mathrm{cc},3}^{\mathrm{II},i} - \psi_{\mathrm{cc},1}^{\mathrm{II},i}\psi_{\mathrm{a},3}^{\mathrm{I}}) \\
&- q_{14}^{12,i}(\psi_{\mathrm{a},2}^{\mathrm{I}}\psi_{\mathrm{cc},3}^{\mathrm{II},i} - \psi_{\mathrm{cc},2}^{\mathrm{II},i}\psi_{\mathrm{a},3}^{\mathrm{I}}) - q_{23}^{12,i}\psi_{\mathrm{a},1}^{\mathrm{I}}\psi_{\mathrm{cc},4}^{\mathrm{II},i}] \\
&\times (-q_{12}^{12,i}\psi_{\mathrm{cc},3}^{\mathrm{II},i} + q_{13}^{12,i}\psi_{\mathrm{cc},2}^{\mathrm{II},i} - q_{23}^{12,i}\psi_{\mathrm{cc},1}^{\mathrm{II},i})^{-1} - \psi_{\mathrm{a},4}^{\mathrm{I}}\} \\
&\times \{[(\psi_{\mathrm{a},1}^{\mathrm{I}})^2 + (\psi_{\mathrm{a},2}^{\mathrm{I}})^2 + (\psi_{\mathrm{a},3}^{\mathrm{I}})^2]^{1/2}s\}^{-1}.
\end{aligned}$$

Considering the situations of the target on all the positions, the unknown angle δ is

$$\delta = \frac{1}{n}\sum_{i=1}^{n}\delta_i \tag{9}$$

According to Eqs. (4) and (9), the laser plane on the j-th position is given by

$$\begin{aligned}
\Psi_{\mathrm{a}}^j = (&\psi_{\mathrm{a},1}^{\mathrm{I}}, \psi_{\mathrm{a},2}^{\mathrm{I}}, \psi_{\mathrm{a},3}^{\mathrm{I}}, \psi_{\mathrm{a},4}^{\mathrm{I}} + [(\psi_{\mathrm{a},1}^{\mathrm{I}})^2 + (\psi_{\mathrm{a},1}^{\mathrm{I}})^2 \\
&+ (\psi_{\mathrm{a},1}^{\mathrm{I}})^2]^{1/2}s^j\cos\delta)^{\mathrm{T}}
\end{aligned} \tag{10}$$

where s^j is the displacement of the table along the rails.

In the surface reconstruction, the measurement object is located in the view field of the camera. Then the laser plane is driven by the stepper motor to scan the object. Several laser curves are generated from intersections between the laser plane and the object. The k-th 3D point $\mathbf{W}_k^j$ on the intersection curve between the j-th laser plane and the measured object is placed on the laser plane, and satisfies the camera projection

relationship, thus [23]

$$(\boldsymbol{\Psi}_{\mathrm{a}}^{j})^{\mathrm{T}}\mathbf{W}_{k}^{j} = 0 \tag{11}$$

$$\mathrm{K}\mathbf{W}_{k}^{j} = \mathbf{w}_{k}^{j} \tag{12}$$

where $\mathbf{w}_{k}^{j}$ is the projection image point. K is the intrinsic parameter matrix. $\mathbf{W}_{k}^{j}$ is determined by the SVD method [25].

The laser plane and the angle δ are further enhanced by an optimization process, which considers the reconstructed distances in the laser planes on the starting position and the second position. The optimization parameters of the function are the coordinate of the laser plane $\boldsymbol{\Psi}_{\mathrm{a}}^{\mathrm{I}}$ and the angle δ. From Eqs. (11) and (12), the k-th 3D point $\mathbf{W}_{k}^{j}$ on the j-th laser plane is parameterized by $\mathbf{W}_{k}^{j}(\boldsymbol{\Psi}_{\mathrm{a}}^{\mathrm{I}}, \delta)$. The standard distance is generated from two different points $\mathbf{W}_{k}^{j}(\boldsymbol{\Psi}_{\mathrm{a}}^{\mathrm{I}}, \delta)$, $\mathbf{W}_{k-1}^{j}(\boldsymbol{\Psi}_{\mathrm{a}}^{\mathrm{I}}, \delta)$ on the j-th laser plane [26]. In order to model the optimization function, we take the standard distances on both I-and II-laser planes into consideration. Therefore, the points $\mathbf{W}_{k}^{\mathrm{I}}(\boldsymbol{\Psi}_{\mathrm{a}}^{\mathrm{I}})$, $\mathbf{W}_{k-1}^{\mathrm{I}}(\boldsymbol{\Psi}_{\mathrm{a}}^{\mathrm{I}})$ on the laser plane I and $\mathbf{W}_{k}^{\mathrm{II}}(\boldsymbol{\Psi}_{\mathrm{a}}^{\mathrm{I}}, \delta)$, $\mathbf{W}_{k-1}^{\mathrm{II}}(\boldsymbol{\Psi}_{\mathrm{a}}^{\mathrm{I}}, \delta)$ on the laser plane II construct two distances for the optimization function as

$$h(\boldsymbol{\Psi}_{\mathrm{a}}^{\mathrm{I}}, \delta) = \sum_{k=1}^{n} \left\{ \left[\left\| \mathbf{W}_{k}^{\mathrm{II}}(\boldsymbol{\Psi}_{\mathrm{a}}^{\mathrm{I}}, \delta) - \mathbf{W}_{k-1}^{\mathrm{II}}(\boldsymbol{\Psi}_{\mathrm{a}}^{\mathrm{I}}, \delta) \right\| - l_{k} \right]^{2} + \left[\left\| \mathbf{W}_{k}^{\mathrm{I}}(\boldsymbol{\Psi}_{\mathrm{a}}^{\mathrm{I}}) - \mathbf{W}_{k-1}^{\mathrm{I}}(\boldsymbol{\Psi}_{\mathrm{a}}^{\mathrm{I}}) \right\| - l_{k} \right]^{2} \right\} \tag{13}$$

where l_k is the standard distance on the vernier caliper. The optimization solutions of the angle $\hat{\delta}$ and the laser plane $\hat{\boldsymbol{\Psi}}_{\mathrm{a}}^{\mathrm{I}}$ are related to the arguments of the smallest optimization function. Then, the j-th laser plane $\boldsymbol{\Psi}_{\mathrm{a}}^{j}$ is derived from Eq. (10). Thus, the 3D points on the surface are reconstructed by Eqs. (11) and (12).

III. EXPERIMENTS AND DISCUSSIONS

A 2048 × 1536 resolution camera and a 260 mm × 380 mm target covered by 20 mm × 20 mm squares are chosen to perform the reconstruction experiments. The laser projector is positioned on the table of the linear path system. The 57HS56-3004A stepper motor is controlled by the C++ code and digital stepping driver, M542 5.0. The computer sends pulses to the digital stepping driver with the I/O card, PCI8735. The I/O card provides 16 channels. Two channels control the movement velocity of the stepper motor. Two channels control the movement direction of the stepper motor. The accuracy of the step motor movement is 0.01 mm. The reconstruction errors of the laser plane on the first position and the errors of the laser plane on the second position are evaluated by changing the standard distance of the measured object as well as the measurement distance from the object to the camera. The distance between the first laser plane and the second laser plane is 100 mm along the rail. The distance between the two laser planes is determined by the size of the target and also determined by the measurement accuracy. Figure 5 describes the influence of the distance between the two laser planes on the performance of the measurement technology. Laser plane I and laser plane II are projected to the target. The projection points A and B are the boundary points of the target in the horizontal plane. The distance AB relates to the distance between the two laser planes. Points a and b are the projections of point A and point B. The large distance from A to B takes the large projection distance from a to b. In other words, the large distance AB is represented by many pixels in the image. Therefore, the large distance AB benefits for the measurement accuracy. However, as the size of the target is fixed, the laser plane II does not intersect to the target with the increasing distance AB. Hence, considering the size of the target and the measurement accuracy, the distance between the two laser planes is 100 mm in the experiments. The experimental errors are calculated by the initialization reconstruction and the optimization reconstruction. The surfaces of three objects are recovered in the experiments. The experimental results are shown in Fig. 6. The experiment setup is described in Fig. 6(a). The experiment instruments in the reconstruction are explained in Fig. 6(b). Figures 6(c), 6(e) and 6(g) are the measured objects in the test. Figures 6(d), 6(f) and 6(h) are the reconstructed shapes of the objects. The reconstruction results in Figs. 6(c), 6(e) and 6(g) agree with the real shapes of the objects in Figs. 6(d), 6(f) and 6(h), respectively.

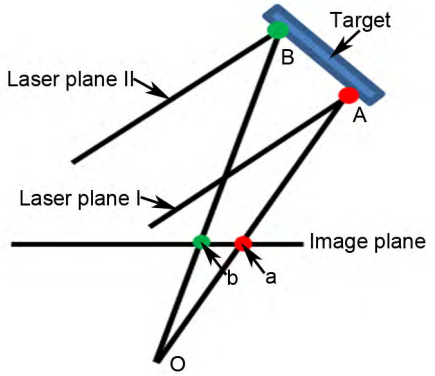

FIGURE 5. The influence of the distance between the two laser planes on the performance of the measurement technology.

For the purpose to quantitively verify the reconstruction errors, the errors of the optimization and initialization are illustrated in Fig. 7 and Fig. 8. The statistical errors on different conditions are listed in Table 1. The experimental errors of the first laser plane are interpreted in Fig. 7. Considering the measurement distance of 500 mm and the standard distances of 20 mm, 40 mm, 60 mm and 80 mm, the averages of the recovery errors of the initialization are 0.68 mm, 0.70 mm, 0.82 mm and 1.44 mm in Fig. 7(a). Furthermore, the averages of the optimization are 0.51 mm, 0.36 mm, 0.55 mm and 0.54 mm. In Fig. 7(b), while the measurement distance climbs to 600 mm, the corresponding error means of the initialization recoveries are 0.73 mm, 0.86 mm, 1.04 mm and 2.24 mm. Then, for the optimization results, the reconstruction errors are 0.54 mm, 0.62 mm, 0.69 mm and 1.23 mm. Fig. 7(c) displays the test results

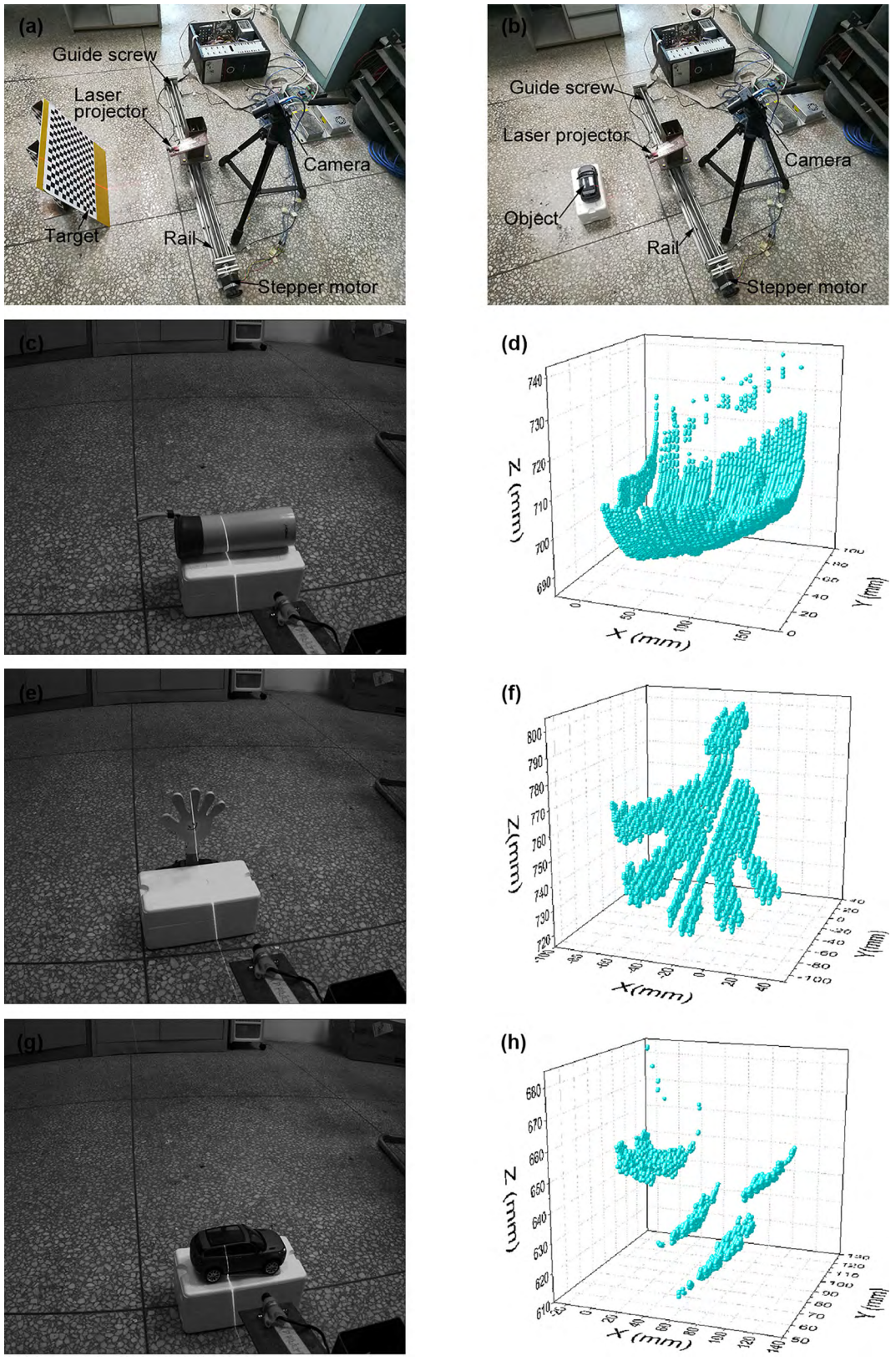

FIGURE 6. Experiment instruments and surface reconstructions of three objects. (a) Experiment instruments in the calibration. (b) Experiment instruments in the reconstruction. (c), (e) and (g) are the three objects measured by the camera-laser-plane system. (d), (f) and (h) are the reconstruction results constructed by the method of the parallel constraint.

TABLE 1. Reconstruction errors adopting the laser planes registered by the parallel constraint.

Measurement distance, mm	Method	Test length, mm							
		Laser plane I				Laser plane II			
		20	40	60	80	20	40	60	80
500	Initialization	0.68	0.70	0.82	1.44	0.81	1.44	1.69	2.66
	Optimization	0.51	0.36	0.55	0.54	0.74	1.11	0.60	0.68
600	Initialization	0.73	0.86	1.04	2.24	0.82	1.61	1.79	2.81
	Optimization	0.54	0.62	0.69	1.23	0.65	0.56	0.53	0.83
700	Initialization	0.87	0.95	1.09	4.00	0.99	2.10	3.26	3.82
	Optimization	0.78	0.81	0.92	1.12	0.76	0.65	0.59	1.14
800	Initialization	2.29	2.45	5.60	6.68	1.38	2.92	4.21	4.26
	Optimization	1.15	1.17	1.26	0.88	0.69	1.04	0.61	0.90

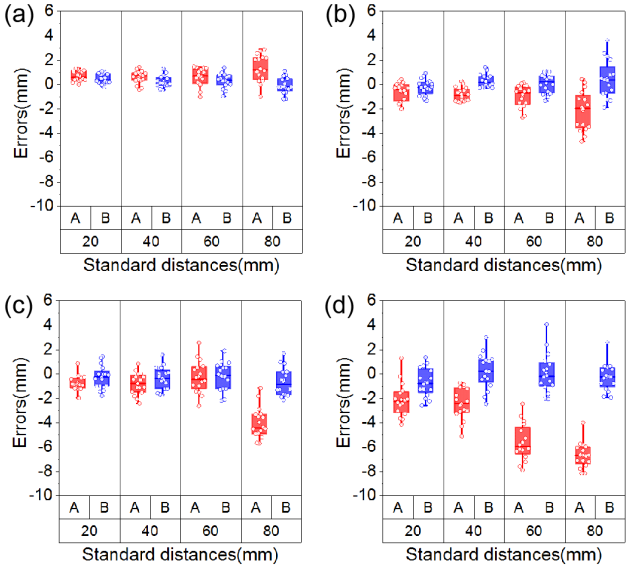

FIGURE 7. Reconstruction errors of the standard distances on the first laser plane that is contributed by the linear path system and registered by the parallel constraint in the verification experiments. "A" and "B" along the *x*-axis indicate the initialization and the optimization methods, respectively. (a), (b), (c) and (d) express the errors of the measurement distances of 500 mm, 600 mm, 700 mm and 800 mm.

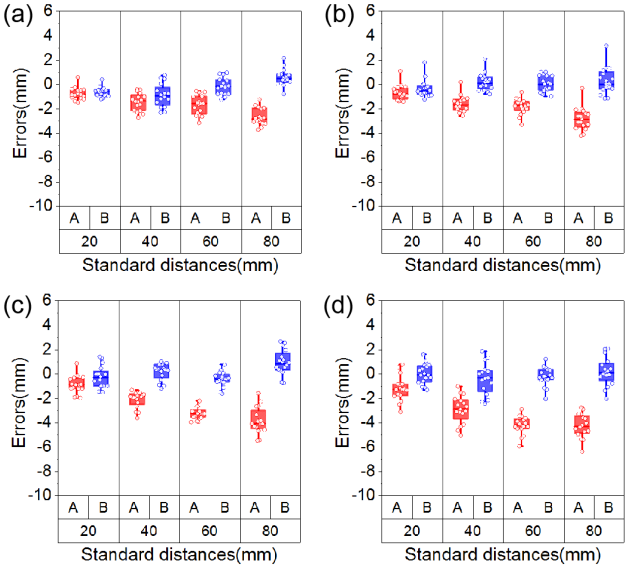

FIGURE 8. Reconstruction errors of the standard distances on the second laser plane that is contributed by the linear path system and registered by the parallel constraint in the verification experiments. "A" and "B" along the *x*-axis indicate the initialization and the optimization methods, respectively. (a), (b), (c) and (d) express the errors of the measurement distances of 500 mm, 600 mm, 700 mm and 800 mm.

that are achieved by the measurement distance of 700 mm and the same standard distances. The error averages of the recoveries are 0.87 mm, 0.95 mm, 1.09 mm and 4.00 mm in initialization method. The corresponding means are 0.78 mm, 0.81 mm, 0.92 mm and 1.12 mm in optimization method. For the measurement distance of 800 mm, the related averages of the initialization method are 2.29 mm, 2.45 mm, 5.60 mm and 6.68 mm in Fig. 7(d). Besides, the error averages of the optimization are 1.15 mm, 1.17 mm, 1.26 mm and 0.88 mm.

In the first group of experiments, when the standard distance is a constant, with the measurement distance growing up from 500 mm to 800 mm, the reconstruction errors of experiments evidently increase in the initialization method. In particular, a significant jump of the errors is observed while the measurement distance rises from 700 mm to 800 mm. For the constant measurement distance, the errors grow up as the standard distance increases from 20 mm to 80 mm in the initialization method gradually. The smallest errors are observed for the standard distance of 20 mm and the measurement distance of 500 mm in the initialization method.

Figure 8 shows the reconstruction errors of the laser plane on the second position. Based on the measurement distance of 500 mm and standard distances of 20 mm, 40 mm, 60 mm and 80 mm, the error means are 0.81 mm, 1.44 mm, 1.69 mm and 2.66 mm in the initialization method in Fig. 8(a). The corresponding errors are 0.74 mm, 1.11 mm, 0.60 mm and 0.68 mm in the optimization method. With respect to the measurement distance of 600 mm, the error means of the initialization are 0.82 mm, 1.61 mm, 1.79 mm and 2.81 mm in Fig. 8(b). Relatively, the means of reconstruction errors are 0.65 mm, 0.56 mm, 0.53 mm and 0.83 mm in the optimization method. Figure 8(c) indicates the experiments that are performed by the measurement distance of 700 mm and the standard distances of 20 mm, 40mm, 60 mm and 80 mm. The error means of the reconstructions are 0.99 mm, 2.10 mm, 3.26 mm and 3.82 mm in the initialization method.

The corresponding error means are 0.76 mm, 0.65 mm, 0.59 mm and 1.14 mm in the optimization method. For the measurement distance of 800 mm in Fig. 8(d), the error means of the initialization method are 1.38 mm, 2.92 mm, 4.21 mm and 4.26 mm. Furthermore, the error averages of the optimization are 0.69 mm, 1.04 mm, 0.61 mm and 0.90 mm.

For the measurement distance of 500 mm and 600 mm, the recovery errors of the laser plane I are overall smaller than those of the laser plane II. While for the measurement distance of 700 mm and 800 mm, the opposite situation can be found. We explain the possible reasons by Fig. 9. In Fig. 9, the laser planes I and II are demonstrated by two parallel lines in the horizontal plane. The four dash lines stand for the planes with measurement distances from 500 mm-800 mm in the horizontal plane. In the horizontal plane, the line segment of the test length is projected to a point. Then, A_{500}, A_{600}, A_{700}, A_{800} are the test places in the laser plane I with the measurement distances from 500 mm-800 mm. B_{500}, B_{600}, B_{700}, B_{800} are the test places on the laser plane II with the measurement distances from 500 mm-800 mm. The test places A_{500}, A_{600}, A_{700}, A_{800}, B_{500}, B_{600}, B_{700}, B_{800} are projected to a_{500}, a_{600}, a_{700}, a_{800}, b_{500}, b_{600}, b_{700}, b_{800} in the image plane. The red center plane passes the optical center O and is vertical to the image plane. As the pixels near the center plane are more accurate than the pixels away from the center plane, The projections a_{500}, a_{600}, b_{700}, b_{800} are more accurate than the corresponding projections b_{500}, b_{600}, a_{700}, a_{800}, respectively. Therefore, for the measurement distance of 500 mm and 600 mm, the recovery errors of the laser plane I are smaller than those of the laser plane II. For the measurement distance of 700 mm and 800 mm, the recovery errors of the laser plane I are larger than those of the laser plane II.

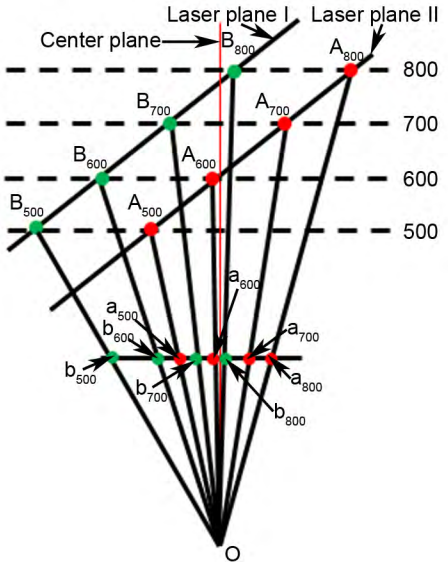

FIGURE 9. The projection principle of the reconstruction test by the method of the parallel constraint.

Figure 8 shows that all the blue error bars are much closer to zero than the red error bars. Therefore, the optimization method effectively reduces the experimental errors and improves the accuracy of the object reconstruction. In addition, for the initialization method, the errors of the reconstruction experiments obviously grow up when the measurement distance rises from 500 mm to 800 mm. For the constant measurement distance, the errors of reconstruction experiments gradually increase as the standard distances increase from 20 mm to 80 mm in the initialization method. The smallest errorsare achieved with the standard distance of 20 mm and the measurement distance of 500 mm in the initialization method.

In summary, in the test of the laser plane on the first position, the measurement distance increases from 500 mm to 800 mm with the interval of 100 mm. The error means of are 0.91 mm, 1.22 mm, 1.73 mm and 4.26 mm in the initialization method and 0.49 mm, 0.77 mm, 0.91 mm and 1.12 mm in the optimization method. Thus, the reconstruction errors increase when the measurement distance goes up. It's worth noting that the errors climb up while the measurement distance is 800 mm in the initialization method. When the standard distance increases from 20 mm to 80 mm with the interval of 20 mm, the error means are 1.14 mm, 1.24 mm, 2.13 mm and 3.59 mm in the initialization method and 0.74 mm, 0.74 mm, 0.85 mm and 0.94 mm in the optimization method. Hence, the errors of reconstruction experiments gradually ascend with the increasing standard distance. Moreover, in the experimental results of the second laser plane, the error means are 1.65 mm, 1.76 mm, 2.54 mm and 3.19 mm in the initialization method and 0.78 mm, 0.64 mm, 078 mm and 0.81 mm in the optimization method. The errors obviously increase in the initialization method when the measurement distance increases from 500 mm to 800 mm. For the increasing standard distance from 20 mm to 80 mm, the error means are 1.00 mm, 2.02 mm, 2.74 mm and 3.39 mm in the initialization method and 0.71 mm, 0.84 mm, 0.58 mm and 0.89 mm in the optimization method. Therefore, the errors of reconstruction experiments gradually increase as the standard distances increase from 20 mm to 80 mm in the initialization method. However, there is no such trend for the reconstruction errors in the optimization method. The reason is that the two laser planes are simultaneously optimized by Eq. (13). The optimization process minimizes the reconstruction errors in the two laser planes and also balances the error distributions in the two laser planes. Thus, the error distribution generated from the optimization method is different from the one generated from the initialization method.

IV. CONCLUSION

A surface reconstruction approach is contributed from the parallel constraint between two laser planes, which are created by a laser projector on a linear path system. The paper also studies the effects of measurement distances and standard distances on the reconstruction errors. The optimization and the initialization methods are evaluated by the

reconstruction errors under different test conditions. The error mean of the initialization method is 2.16 mm. The error mean of the optimization method is 0.78 mm in the experiments. The experimental results from the optimization are much smaller than the errors obtained by the initialization method, which suggests the potential applications in the surface inspection fields.

REFERENCES

[1] E. Bae, Y. Kim, S. Park, and S.-W. Kim, "Large-aperture ground glass surface profile measurement using coherence scanning interferometry," *Opt. Express*, vol. 25, no. 2, pp. 1106–1113, 2017.
[2] H. M. Park, H. W. Jung, and K.-N. Joo, "Dual low coherence scanning interferometry for rapid large step height and thickness measurements," *Opt. Express*, vol. 24, no. 25, pp. 28625–28632, 2016.
[3] K. Sridharan and R. Sivaramakrishnan, "Compression and deformation of cylindrical rubber blocks," *MAPAN*, vol. 29, no. 2, pp. 107–114, 2014.
[4] G. Xu, J. Yuan, X. Li, and J. Su, "Profile reconstruction method adopting parameterized re-projection errors of laser lines generated from bi-cuboid references," *Opt. Express*, vol. 25, no. 24, pp. 29746–29760, 2017.
[5] B. Štrbac, V. Radlovački, V. Spasić-Jokić, M. Delić, and M. Hadžistević, "The difference between GUM and ISO/TC 15530-3 method to evaluate the measurement uncertainty of flatness by a CMM," *MAPAN*, vol. 32, no. 4, pp. 251–257, 2017.
[6] P. Marcon, K. Bartusek, M. Burdkova, and Z. Dokoupil, "Magnetic susceptibility measurement using 2D magnetic resonance imaging," *Meas. Sci. Technol.*, vol. 22, no. 10, p. 105702, 2011.
[7] J. Mikulka, E. Gescheidtova, and K. Bartusek, "Soft-tissues image processing: Comparison of traditional segmentation methods with 2D active contour methods," *Meas. Sci. Rev.*, vol. 12, no. 4, pp. 153–161, 2012.
[8] J. Lu and H. Zhou, "Numerical reproduction and explanation of road surface mirages under grazing-angle scattering," *Appl. Opt.*, vol. 56, no. 19, pp. 5550–5558, 2017.
[9] A. Glowacz and Z. Glowacz, "Diagnosis of the three-phase induction motor using thermal imaging," *Infr. Phys. Technol.*, vol. 81, pp. 7–16, Mar. 2016.
[10] Y.-T. Park and D.-H. Lee, "3D vision-based security monitoring for railroad stations," *J. Opt. Soc. Korea*, vol. 14, no. 4, pp. 451–457, 2010.
[11] R. A. Hamzah and H. Ibrahim, "Literature survey on stereo vision disparity map algorithms," *J. Sensors*, vol. 2016, Nov. 2016, Art. no. 8742920.
[12] H. Kieu, T. Pan, Z. Wang, M. Le, H. Nguyen, and M. Vo, "Accurate 3D shape measurement of multiple separate objects with stereo vision," *Meas. Sci. Technol.*, vol. 25, no. 3, p. 035401, 2014.
[13] D. G. Lowe, "Distinctive image features from scale-invariant keypoints," *Int. J. Comput. Vis.*, vol. 60, no. 2, pp. 91–110, 2004.
[14] P. Sandoz, J. E. Meneses, M. A. Suarez, and T. Gharbi, "3D localization of a labeled target by means of a stereo vision configuration with subvoxel resolution," *Opt. Express*, vol. 18, no. 23, pp. 24152–24162, 2010.
[15] X. Shao, X. Dai, Z. Chen, Y. Dai, S. Dong, and X. He, "Calibration of stereo-digital image correlation for deformation measurement of large engineering components," *Meas. Sci. Technol.*, vol. 27, no. 12, p. 125010, 2016.
[16] Z. Luo, K. Zhang, Z. Wang, J. Zheng, and Y. Chen, "3D pose estimation of large and complicated workpieces based on binocular stereo vision," *Appl. Opt.*, vol. 56, no. 24, pp. 6822–6836, 2017.
[17] T. Bell, B. Vlahov, J. P. Allebach, and S. Zhang, "Three-dimensional range geometry compression via phase encoding," *Appl. Opt.*, vol. 56, no. 33, pp. 9285–9292, 2017.
[18] P. de Groot, J. Biegen, J. Clark, X. C. de Lega, and D. Grigg, "Optical interferometry for measurement of the geometric dimensions of industrial parts," *Appl. Opt.*, vol. 41, no. 19, pp. 3853–3860, 2002.
[19] X. Huang *et al.*, "Polarimetric target depth sensing in ambient illumination based on polarization-coded structured light," *Appl. Opt.*, vol. 56, no. 27, pp. 7741–7748, 2017.
[20] B.-Q. Shi and J. Liang, "Guide to quickly build high-quality three-dimensional models with a structured light range scanner," *Appl. Opt.*, vol. 55, no. 36, pp. 10158–10169, 2016.
[21] Y. Villa, M. Araiza, D. Alaniz, R. Ivanov, and M. Ortiz, "Transformation of phase to (x, y, z)-coordinates for the calibration of a fringe projection profilometer," *Opt. Laser Eng.*, vol. 50, no. 2, pp. 256–261, 2012.
[22] Q. Hu, P. S. Huang, Q. Fu, and F.-P. Chiang, "Calibration of a three-dimensional shape measurement system," *Opt. Eng.*, vol. 42 no. 2, pp. 487–493, 2003.
[23] G. Xu, X. Zhang, J. Su, X. Li, and A. Zheng, "Solution approach of a laser plane based on Plücker matrices of the projective lines on a flexible 2D target," *Appl. Opt.*, vol. 55, no. 10, pp. 2653–2656, 2016.
[24] Z. Zhang, "A flexible new technique for camera calibration," *IEEE Trans. Pattern Anal. Mach. Intell.*, vol. 22, no. 11, pp. 1330–1334, Nov. 2000.
[25] R. Hartley and A. Zisserman, *Multiple View Geometry in Computer Vision*. Cambridge, U.K.: Cambridge Univ. Press, 2003.
[26] G. Xu, J. Yuan, X. Li, and J. Su, "Optimization reconstruction method of object profile using flexible laser plane and bi-planar references," *Sci. Rep.*, vol. 8, no. 1, 2018, Art. no. 1526.

GUAN XU was born in Changchun, Jilin, China, in 1981. He received the B.S., M.S., and Ph.D. degrees in vehicle operation engineering from Jilin University, Jilin, in 2003, 2006, and 2009, respectively. His research interests include active vision and stereo vision in vehicle inspection techniques.

FANG CHEN was born in Shaoxing, Zhejiang, in 1994. She received the B.S. degree in automobile support engineering from the Ningbo University of Technology, Zhejiang, China, in 2017. Her research interests include active vision and 3-D reconstruction in vehicle inspection techniques.

XIAOTAO LI was born in Changchun, Jilin, China, in 1980. She received the B.S., M.S., and Ph.D. degrees in mechanical engineering from Jilin University, Jilin, in 2010. Her research interests include vision-based measurement and MEMS.

JUNYI CHEN was born in Jilin City, China, in 1995. She received the B.S. degree in vehicle operation engineering from Jilin University, Jilin, in 2017. Her research interests include active vision and stereo vision in vehicle inspection techniques.